Charge transfer in mixed and segregated stacks of tetrathiafulvalene, tetrathianaphthalene and naphthalene diimide: a structural, spectroscopic and computational study

Journal:	*New Journal of Chemistry*
Manuscript ID	NJ-ART-02-2022-000643.R1
Article Type:	Paper
Date Submitted by the Author:	08-Apr-2022
Complete List of Authors:	Leong, Chanel; University of Sydney, Chemistry Chan, Bun; Nagasaki University, Graduate School of Engineering Liu, Tianfu; a. State Key Laboratory of Structural Chemistry, Fujian Institute of Research on the Structure of Matter, Chinese Academy of Sciences, ; Moore, Harrison; The University of Sydney, School of Chemistry Hod, Idan; Ben-Gurion University of the Negev, Chemistry Solomon, Marcello; The University of Sydney, Chemistry Usov, Pavel; The University of Sydney, Chemistry Hupp, Joseph; Northwestern University, Department of Chemistry Farha, Omar; Northwestern University, Chemistry D'Alessandro, Deanna; The University of Sydney, School of Chemistry

SCHOLARONE™
Manuscripts

Charge transfer in mixed and segregated stacks of tetrathiafulvalene, tetrathianaphthalene and naphthalene diimide: a structural, spectroscopic and computational study

Chanel F. Leong,[a] Bun Chan,[b] Tianfu Liu,[c] Harrison S. Moore,[a] Idan Hod,[d] Marcello B. Solomon,[a] Pavel M. Usov,[a] Joseph T. Hupp,[c] Omar Farha,[c] Deanna M. D'Alessandro[a*]

[a] *School of Chemistry, The University of Sydney, New South Wales 2006, Australia*

[b] *Graduate School of Engineering, Nagasaki University, Bunkyo 1-14, Nagasaki 852-8521, Japan*

[c] *Department of Chemistry, Northwestern University, Evanston, Illinois 60208-3113, USA*

[d] *Department of Chemistry and Ilse Katz Institute for Nanoscale Science and Technology, Ben-Gurion University of the Negev Beer-Sheva, 8410501, Israel*

The authors would like to dedicate this work to Professor Peter Junk on the occasion of his 60th birthday.

ABSTRACT

Tetrathiafulvalene (TTF) is a highly tunable electron donor that has been widely studied in charge transfer (CT) complexes, including Bechgaard salts which are superconductors at low temperatures. Its close relative, tetrathianaphthalene (TTN) has received considerably less attention than its TTF counterpart but is potentially a versatile electron donor. Three novel CT complexes are reported, containing mixed and segregated stack donor-acceptor (D–A) complexes of tetrathiafulvalene (TTF), tetrathianaphthalene (TTN) and naphthalene diimide (NDI). We report a facile mechanochemical synthesis of two salts, TTF-DPNI and TTN-DPNI (DPNI = *N,N′*-Di-(4-pyridyl)-1,4,5,8-naphthalenetetracarboxydiimide), which is uncommon for these materials. Despite the detection of a very low partial charge transfer in the three salts using UV-Vis-NIR, Raman and EPR spectroscopies, we elucidated the properties of the TTN core with support from DFT calculations for the first time. We highlight the performance of TTN in a CT complex and demonstrate the importance of a combined approach to the characterisation of CT in organic D–A complexes.

INTRODUCTION

The bountiful literature on organic donor-acceptor (D–A) charge transfer (CT) complexes, or 'organic metals,' has revealed their unprecedented electronic properties.[1-4] The discovery of the CT complex tetrathiafulvalene-tetracyanoquinodimethane (TTF-TCNQ) in 1973, which exhibited metallic conductivity comparable to copper (1.47×10^4 S cm^{-1} *vs.* 6×10^5 S cm^{-1}),[5] inspired a movement towards the development of organic conductors and superconductors.[6] Organic CT complexes hold significant promise in the development of high performance devices by virtue of their excellent electrical properties, low contact resistance, and tuneable metal Fermi energies.

Owing to its excellent electron donating ability, tetrathiafulvalene (TTF) (Figure 1) and TTF-based compounds have been widely employed as electron donors in organic CT complexes.[7-9] Systematic studies by Torrance and co-workers led to the development of the 'V-shaped diagram,' which revealed a relationship between the relative oxidation and reduction potentials of donor and acceptor units, respectively, and the energy of the charge transfer band in mixed-stack CT complexes.[10] This theory enabled engineering of CT complexes with desired electronic properties by judicious choice of donors and acceptors by means of their redox properties.[4] TTF is of further interest due to its facile incorporation into organic CT complexes mechanochemically,[11] which is favourable for large scale syntheses and applications. It is well documented that TTF forms CT complexes when mechanochemically combined with chloranil,[12-14] iodide salts[15] and TCNO;[16] however, mechanochemical syntheses with DPNI-based ligands are less well studied.

An interesting property of TTF CT complexes is their potential to exhibit dichroism due to their stacking motif. Polarised single crystal transmission UV–Vis–NIR spectroscopy is a technique gaining attention for its capability to measure a UV–Vis–NIR spectrum based on a single orientation of the crystal structure. It fundamentally varies from diffuse reflectance UV–Vis–NIR spectroscopy, which measures an average of all possible crystal orientations. A further advantage in measuring a single crystal over a bulk powder is the reduction of inhomogeneous broadening leading to better resolved spectra.[17, 18] Single crystal transmission UV–Vis–NIR spectroscopy has been used to quantify solid state intervalence charge transfer,[19] but can be applied to observe dichroism.

Tetrathianaphthalene (TTN; or tetrathiatetralin) is a structural isomer of TTF (Figure 2). Despite its similarity to TTF, it has received lesser attention in this field due to its weaker electron donating ability and non-planar geometry.[20] Reports of TTN-based CT complexes remain limited, and include a TTN-I_2 salt exhibiting pressure-dependent conductivity of 1×10^{-5}–1×10^{-3} S cm^{-1} in the pressure range 0.25–8 GPa,[21] and co-crystals of aryl-fused TTN analogues with fullerenes C_{60} and C_{70}.[22] In the latter cases, the aryl-fused systems formed D–A CT complexes more readily due to their lower oxidation potentials compared to TTN alone; however, their optical spectra did not show evidence of low energy CT transitions. To the best of our knowledge, no crystal structures of TTN CT complexes have been reported to date and there is no indication that these complexes can be synthesised mechanochemically.

Naphthalene diimide (NDI) (Figure 1) is a well-known electron acceptor that has been investigated as an acceptor in organic CT complexes,[23-25] higher dimensional D–A supramolecular assemblies,[26] anion–π complexes,[27] and D–A Metal-Organic Frameworks (MOFs).[28] Its low-lying lowest unoccupied molecular orbital (LUMO) and large planar π-system has led to a number of reports of CT complexes with small planar molecules such as benzene derivatives,[24, 29] dialkoxynaphthalenes[23] and naphthalene derivatives.[30, 31] Furthermore, the amenability of the NDI to core functionalisation, which directly tunes its LUMO energy, provides an excellent handle for tuning its electron accepting ability.

Herein, we report the solution and mechanochemical syntheses of three novel D–A CT complexes with 1:1 stoichiometry: a mixed stack TTF-DPNI CT complex (α-TTF-DPNI; DPNI = *N,N′*-di-(4-pyridyl)-1,4,5,8-naphthalenetetracarboxydiimide), a segregated stack TTF-DPNI CT complex (β-TTF-DPNI) and an isomorphic segregated stack CT complex, TTN-DPNI. The structures of these CT complexes were first elucidated, then the optical and vibrational properties of the materials probed by bulk and single crystal solid state UV-Vis-NIR, Raman and Electron Paramagnetic Resonance (EPR) spectroscopies. Finally, the experimentally observed behaviours were supported with density functional theory (DFT) calculations to elucidate the degree of CT within these complexes.

EXPERIMENTAL

General. All reagents and solvents were purchased from commercial suppliers and used without further purification unless otherwise stated. CS_2 was distilled over CaH_2 prior to its use. TTF (97%) was purchased from Accela and used without further purification.

Syntheses

_N,N′_-Di-(4-pyridyl)-1,4,5,8-naphthalenetetracarboxydiimide **(DPNI):** DPNI was synthesised _via_ a modified literature procedure.[32] 4-Aminopyridine (1.18 g, 12.6 mmol) was added to a stirring solution of 1,4,5,8-naphthalenetetracarboxylic dianhydride (1.35 g, 5.03 mmol) in anhydrous DMF (20 mL) under a flowing N_2 atmosphere. The solution was heated at 130 °C overnight with stirring under N_2. The solution was cooled to 0 °C to precipitate a beige solid. The product was isolated by vacuum filtration, rinsed with DMF and acetone until the washings were colourless then dried. Yield: 2.05 g, 97%. ^{1}H NMR (200 MHz, _d_-TFA): $\delta = 8.43$ (d, $J_{H-H} = 0.02$, 4H), 9.07 (s, 4H), 9.15 (d, $J_{H-H} = 0.03$, 4H) ppm. The characterisation data matched that previously reported.[32]

Tetrathianaphthalene (TTN): TTN was synthesised _via_ a modified literature procedure.[33] Sodium metal (0.50 g, 22 mmol) and CS_2 (4.00 mL, 66 mmol) were refluxed under N_2. DMF (5 mL) was added dropwise over 30 min to the refluxing solution. The mixture was then allowed to reflux for an additional 2 h, whereby a colour change in the solution from colourless to deep red was observed. DMF was removed _via_ distillation to yield the crude diethyl thiolate salt as a deep red residue, which was used in the next step without further purification.

Sodium ethoxide (30 mL, 3.77 M) in THF (200 mL) was brought to reflux. A solution of _cis_-1,2-dichloroethylene (1.66 mL, 22 mmol) in THF (70 mL) and the crude diethyl thiolate salt in THF (70 mL) were added dropwise to the refluxing solution over 1 h. The solution was refluxed overnight under N_2. The mixture was poured into ice-water (500 mL) and brine (100 mL) was added to the resulting slurry. Orange/brown crystals of crude TTN formed from the solution, which were isolated by vacuum filtration and rinsed with water. Crude TTN was purified by flash chromatography (silica, DCM) to yield light brown crystals. Yield = 0.94 g, 42% (compared to Na). ^{1}H NMR (300 MHz, d_6-DMSO): $\delta = 6.75$ (s, 4H) ppm. The characterisation data matched that previously reported.[33]

TTF-DPNI and TTN-DPNI:

Solution Preparation: The donor (either TTF or TTN (8.00 mg, 0.04 mmol)) and the acceptor (DPNI (16.0 mg, 0.04 mmol)) were separately dissolved in hot acetonitrile (1.5 mL each). The donor and acceptor solutions were combined whilst hot. The resulting mixture was capped and allowed to crystallise at 17 °C. Dark green rectangular and prismatic blocks of α-TTF-DPNI

and β-TTF-DPNI, respectively, formed over one week. Black diamondoid crystals of TTN-DPNI formed over the period of a week.

Mechanochemical Preparation: The donor (either TTF or TTN (20.0 mg, 0.098 mmol)) and the acceptor (DPNI (41.0 mg, 0.098 mmol))) were ground together for 15-20 minutes. TTF-DPNI was produced as a bright green powder, while TTN-DPNI was produced as a black powder.

Characterisation techniques

Powder X-ray Diffraction. Powder X-ray diffraction data on powdered CT complexes were collected on a Rigaku ATXG Diffractometer in the 2θ range of 2-35° at 3° step size and scan rate of 5° min^{-1}. Samples were adhered to a rough glass substrate and appended onto a static sample stage.

Single Crystal X-Ray Diffraction.

α-TTF-DPNI: A single crystal of TTF-DPNI was mounted on a 20 μm nylon loop with Paratone *N* oil and cooled to 150 K using an Oxford Cryostream. Diffraction data was collected on a Bruker Apex II Prospector diffractometer, which employed Cu-Kα (λ = 1.54178 Å) radiation. The data was processed using SAINT[34] on the APEX2 software suite, and subsequent computations were performed using SHELXS-86[35] and SHELXL[36] on the Olex2 interface.[37] Non-hydrogen atoms were modelled with anisotropic displacement parameters and hydrogen atoms were refined with a riding atom model.

β-TTF-DPNI: A single crystal of β-TTF-DPNI was mounted onto a 20 μm nylon loop with Paratone *N* oil and quenched in a N_2 stream at 150 K using an Oxford Cryostream. Diffraction data was collected on a SuperNova Dual Atlas diffractometer employing Cu-Kα (λ = 1.54178 Å) radiation. Data reduction and integration were performed on the CrysAlisPro software package.[38] Structure solution and refinement was achieved using SHELXS-86[35] and SHELXL-2014/7,[36] respectively, on the WinGX graphical user interface.[39] A multi-scan absorption correction was applied using the SCALE3 ABSPACK[40] scaling algorithm. All non-hydrogen atoms were modelled with anisotropic displacement parameters and hydrogen atoms were refined isotropically with a riding atom model.

TTN-DPNI: A single crystal of TTN-DPNI was mounted onto a 20 μm nylon loop with Paratone *N* oil and cooled to 299 K using an Oxford Cryostream. Data was collected on a Bruker Apex II Prospector diffractometer employing Cu-Kα radiation (λ = 1.54178 Å), and was processed *via* SAINT[34] on the APEX2 software suite. Subsequent computations were performed using SHELXS-86[35] and SHELXL[36] on the Olex2 interface.[37] Non-hydrogen atoms were modelled with anisotropic displacement parameters and hydrogen atoms were refined with a riding atom model.

Electrochemistry. DC cyclic voltammetry (CV) was performed using a BASi Epsilon Electrochemical Analyser potentiostat in a three-electrode cell. The electrodes employed were a glassy carbon working electrode (1.5 mm diameter), a Pt wire auxiliary electrode, and a Ag/Ag$^+$ *quasi*-reference electrode. The electrolyte ([(n-C$_4$H$_9$)$_4$N]PF$_6$ (0.1 M) in DMF) was degassed under a flow of high purity Ar gas prior to measurements. A full potential sweep was first performed on the electrolyte to detect any impurities in the cell. The sample was introduced by dissolving the sample (1-2 mg) into the electrolyte. Ferrocene was added as an internal reference at the conclusion of each experiment. All potentials are reported in V and referenced to the ferrocene/ferrocenium (Fc/Fc$^+$) couple.

Diffuse Reflectance UV-Vis-NIR Spectroscopy. UV-Vis-NIR spectra were collected on a CARY5000 spectrophotometer equipped with a Harrick Praying Mantis™ attachment, interfaced to Varian WinUV software. Solid, powdered samples were prepared in a dry BaSO$_4$ matrix, upon which the background was collected. Spectra were collected in the range 5000 to 40000 cm^{-1} at a scan rate of 6000 cm^{-1} min^{-1}.

Single Crystal Vis-NIR Spectroscopy. Polarised single crystal Vis-NIR spectra were collected on a customised spectrophotometer designed by Krausz.[17] The instrument is composed of optics obtained from a CARY14 spectrophotometer equipped with a 24 V/150 W quartz halogen lamp and a Spec 1704, 1 m, high-resolution Czerny-Turner monochromator and a high-speed stepper motor. A single crystal was mounted over a 1 mm aperture and data were collected in both horizontal and vertical polarisation modes. For visible spectra, a grating blazed at 500 nm was used in conjunction with an EMI 9659QB Photomultiplier Tube. Spectra were then collected in the range 350 to 750 nm (13330-28570 cm^{-1}) in 10 nm increments. For NIR spectra, a grating blazed at 1000 nm was used in conjunction with an OSRAM BXP-65 Silicon PIN Photodiode. Spectra were collected in the range 700 to 1100 nm

(9090-14290 cm^{-1}) in 10 nm increments. A baseline correction was applied to the data by measuring the absorbance spectrum of the empty aperture, which was then manually subtracted from the absorption spectrum of the crystal. All spectra were collected using two orthogonal polarisations. These have been labelled as '0 degrees' and '90 degrees' and do not reflect the absolute orientations of the crystals.

Electron Paramagnetic Resonance. Continuous wave X-band EPR spectra were collected on a Bruker EMXnano bench-top spectrometer. All samples were prepared mechanochemically and were loaded into quartz tubes. Spectra were obtained at room temperature. The parameters used were: microwave frequency, 9.64 GHz; receiver gain, 60 dB; modulation amplitude, 1.0 G; attenuation, 25 dB; sweep width, 50 G; sweep time, 20.12 s; accumulations, 20.

Confocal Raman Spectroscopy. Raman spectra were obtained using a Renishaw Raman inVia Reflex Spectrometer equipped with a Leica DMLM microscope. Excitation lasers of wavelength 785 nm were employed. Data were processed using wiRE^{TM} software.

Two-Probe Conductivity. Pellets of powdered sample (approx. 40 mg) were prepared using a pellet press (7.14 mm diameter) at an applied pressure of 0.25 tonnes. Conductive silver epoxy (1 cm width) was applied across the conductive face of two Fluorinated-Tin-Oxide (FTO) plates (approximate dimensions 3 × 1.5 cm). The pellet was adhered between these two FTO plates, ensuring the two faces of the pellet were in complete contact with the silver epoxy. The cell was connected to an AMETEK Solartron Analytical Modulab Potentiostat and potential sweeps were performed across the range 3 to −3 V at a sweep rate of 10 mV s^{-1}.

Computational Methods. Standard computational chemistry and density functional theory (DFT)[41] computations were carried out with Gaussian 16.[42] For model complexes of TTF/TTN and DPNI, the geometries were extracted from the experimental crystal structures without modification. For the monomeric donor and acceptor species, the geometries were optimised at the B3LYP/6-31+G(d,p) level,[43] which is widely used for this purpose and is a component for a range of high-level composite methods.[44, 45] Vibrational frequencies and the associated IR and Raman intensities were obtained at the same level of theory. Improved single-point energies were obtained at the M06-2X/6-311+G(3df,2p) level for the calculation of thermochemical quantities (ionization potentials and electron affinities).[46] The M06-2X have been shown to be highly accurate for a wide range of thermochemical properties including IPs and EAs.[47] Simulated UV-Vis-NIR were obtained using the TDA-BMK/6-31G(d) method,[48,]

[49] which has been previously applied to related systems and has shown to yield reliable qualitative characteristics as well as semi-quantitative excitation energies.[50, 51]

RESULTS AND DISCUSSION

Co-crystallisation of TTF/TTN and DPNI. Deep green crystals of TTF-DPNI were crystallised from a hot stoichiometric mixture in acetone after being left for one week in a temperature-controlled environment (*ca.* 17 °C). Two different morphologies of TTF-DPNI were formed, corresponding to rectangular, needle-like blocks of α-TTF-DPNI and truncated, diamondoid prisms of β-TTF-DPNI. The α-phase exhibits dichroism of pale and deep green upon light polarisation (Figure S1, ESI), which can be accounted for by the directionality of the D–A stacks (*vide infra*). The β-TTF-DPNI complex does not exhibit dichroism. Lower crystallisation temperatures favoured the growth of α-TTF-DPNI (temperatures below 17 °C), whereas β-TTF-DPNI was the dominant product at temperatures above 17 °C. The TTN core has received considerably less attention than TTF as an electron donor; therefore, TTN-DPNI was crystallised using the same conditions. After one week, black diamondoid blocks of TTN-DPNI had formed, with only a single phase observed. Dichroism was also observed in TTN-DPNI upon plane polarisation (Figure S2, ESI); however, the effects are more subtle and could be attributed to the weaker electron donating ability of the TTN core.

Mixed and segregated stacking motifs TTF-DPNI and TTN-DPNI.

The difference in both phases of TTF-DPNI was confirmed by single crystal X-ray diffraction, which showed variation in the stacking of the TTF moiety.

α-TTF-DPNI. α-TTF-DPNI crystallises in the triclinic crystal system P-1 with unit cell dimensions $a = 11.094$, $b = 11.346$, and $c = 22.454$ Å, $\alpha = 102.51$, $\beta = 97.53$, $\gamma = 100.71°$. Owing to the low symmetry afforded by the triclinic crystal system, the structure is comprised of a large asymmetric unit consisting of two acceptor DPNI molecules (labelled A_1 and A_2), and four TTF half units. There are four crystallographically unique donor TTF molecules (labelled D_1, D_2, D_3 and D_4), which are generated *via* inversion symmetry across the exocyclic central C=C double bond. The TTF and DPNI molecules are arranged in a mixed stack fashion, forming two types of columnar D–A mixed stacks with the motifs: $D_1A_1D_2A_1$ (Stack 1) and $D_3A_2D_4A_2$ (Stack 2) (Figure 1(a)). The stacking distances between D–A are in the range of moderate to strong π-stacking interactions, where D_1–A_1, D_2–A_1, D_3–A_2 and D_4–A_2 are 3.54,

3.52, 3.47 and 3.60 Å, respectively. Stack 1 (blue) and Stack 2 (purple) are arranged adjacent to one another in an alternating fashion forming a striped pattern along the c-axis (Figure 1(b)).
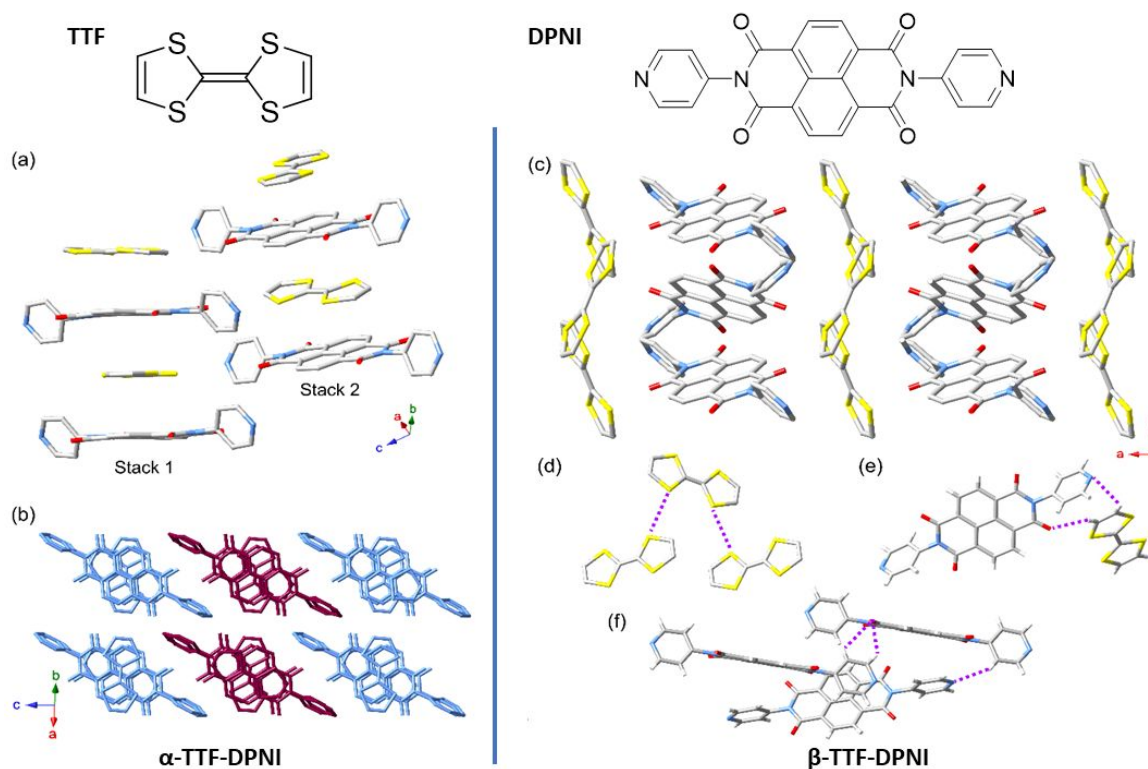
Figure 1. (a) Crystal structure of α-TTF-DPNI showing two crystallographically unique D–A stacks, Stack 1 and Stack 2, and (b) the arrangement of Stack 1 (blue) and Stack 2 (purple) stacks with respect to each other. (c) Crystal structure of β-TTF-DPNI viewed down the c-axis, and the (d) S···S contacts between TTF, (e) hydrogen bonding between TTF and DPNI and (f) hydrogen bonding between adjacent DPNI. Hydrogen atoms omitted for clarity unless otherwise stated. Intermolecular interactions shown as purple broken lines. Colour scheme: N, blue; O, red; C, grey; S, yellow; H, white.

The exocyclic central double bond of TTF is sensitive to the oxidation state of the molecule;[52, 53] therefore, bond length analysis may provide detailed insights into the charge on the TTF unit. When TTF undergoes a one electron oxidation from its neutral to radical cation state, the central double bond shortens as the half unit aromatises and the central double bond gains single bond character. The central C=C bond lengths of D_1, D_2, D_3, and D_4 in α-TTF-DPNI are 1.345, 1.361, 1.357 and 1.344 Å, respectively. A comparison of these values with reported C=C bond lengths

of TTF in numerous D–A complexes of varying degrees of CT (ρ) is consistent with TTF in its neutral state.[52]

β-TTF-DPNI. The second phase, β-TTF-DPNI, crystallised in the monoclinic space group $P\,2_1/c$ with unit cell parameters a = 13.325, b = 8.471, c = 11.824 Å, β = 101.086°. Owing to the higher symmetry afforded by the monoclinic crystal system, the asymmetric unit, comprising of half a TTF and half a DPNI molecule, is smaller than that of the α-phase. The TTF and DPNI units are arranged in a segregated stack fashion, where individual sheets of TTF and DPNI alternate along the *a*-direction, parallel to the *b-c* plane (Figure 1(c)). The β-TTF-DPNI segregated stack CT complex exhibits no obvious π-interactions between D and A moieties, compared to those face-to-face π-stacking interactions observed between TTF and DPNI in α-TTF-DPNI.

The β-TTF-DPNI phase exhibits a number of important interactions that are absent in the α-TTF-DPNI phase. In addition to the π-stacking interactions between the pyridyl and naphthalene aromatic centres on DPNI, there are close S···S contacts (3.591 Å) between TTF molecules (Figure 1(d)). Furthermore, hydrogen bonding interactions between TTF and DPNI were found (Figure 1(e)): N2···H2-C2 (3.213 Å) and O1···H1-C1 (2.497 Å), as well as between DPNI molecules (Figure 1(f)): N2···H5-C5 (2.796 Å), O2···H9-C8 (2.636 Å), and O2···H7-C7 (2.975 Å). The exocyclic C=C bond length of TTF is 1.341 Å which, like the α-phase, corresponds well with neutral TTF.

TTN-DPNI. Black diamondoid blocks of TTN-DPNI crystallised in the monoclinic space group $P\,2_1/c$, with unit cell parameters a = 14.044, b = 8.232, c = 11.711 Å and β = 103.51°. The structure is isomorphous with β-TTF-DPNI, whereby D and A units are arranged in segregated sheets (Figure 2(a)). The asymmetric unit consists of half a TTN and one DPNI moiety, which generates the full molecules by inversion symmetry. The TTN moieties are relatively positioned in a side-on fashion revealing S···S (S1···S2) contacts of 3.667 Å (Figure 2(c)), which are slightly longer than the S···S contact distances found in β-TTF-DPNI. This likely results from the non-planar chair configuration of the TTN molecules, which hinders the close packing of these donor units due to steric effects (Figure 2(b)).
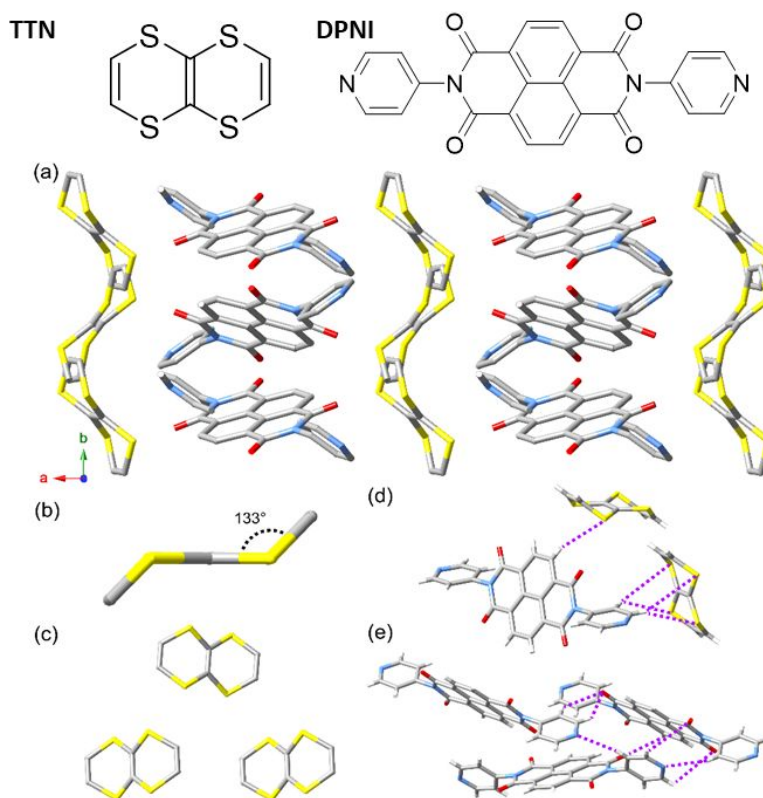
Figure 2. Crystal structure of TTN-DPNI (a) viewed down the crystallographic *c*-axis, and (b) a demonstration of the bent structure of the TTN molecule. Hydrogen atoms omitted for clarity. A close look at the (c) S···S interactions between adjacent TTN units, and hydrogen bonding interactions between (d) DPNI and TTN units and (e) DPNI components. Intermolecular interactions shown as purple broken lines. Hydrogen atoms omitted for clarity unless otherwise stated. Colour scheme: N, blue; O, red; C, grey; H, white; S, yellow.

The TTN molecules adopt a chair configuration, where the central carbon-sulfur functionality (Figure 2) forms the seat which makes dihedral angles of 133° with the outer C=C bonds (Figure 2(b)). The discrete TTN core also adopts a chair conformation; Varma and co-workers reported dihedral angles in the crystal structure of neutral TTN to range between 129.0(5)-131.0(5)°, which is slightly less buckled than reported in TTN-DPNI.[33] The non-planar configuration of TTN renders it non-aromatic. The significance of this angle on the heat of formation of the molecule is minimal as seen from reported computational calculations.[54] The radical cation of TTN, as shown computationally, tends towards a more planar configuration (between dihedral angles of 150-180°), with a greater delocalisation of π and *s* orbitals across the central C_2S_4 subunit. As a result, determination of the charge of TTN

and thus the ρ in this system cannot be purely determined *via* structural analyses; however, given the similarity of the conformation of TTN in TTN-DPNI to TTN, it suggests that TTN may be in its neutral state in this CT complex.

Weak hydrogen bonding interactions were found between TTN and DPNI units, namely O8···H16-C16 (2.5273 Å), S1···H11-C10 (3.201 Å), S1···H1-C1 (3.102 Å), S1···H2-C2 (3.887 Å), S2···H1-C1 (3.606 Å) and S2···H2-C2 (3.516 Å) (Figure 2(d)). Hydrogen bonding interactions between adjacent DPNI acceptors are also present, i.e., N1···H2-C2 (2.813 Å), O1···H1-C1 (3.645 Å), O2···H4-C4 (2.874 Å), O2···H5-C5 (2.755 Å) O2···H5-C5 (4.165 Å), O2···H11-C11 (4.009 Å), and O7···H5-C5 (4.1654 Å) (Figure 2(e)). The intermolecular DPNI hydrogen bonds are, on average, longer than those found in β-TTF-DPNI. No significant π–π interactions were observed between TTN and DPNI moieties, similar to β-TTF-DPNI, which suggests that the CT interaction may be promoted by the local intermolecular interactions between TTN and DPNI moieties.

Mechanochemical preparation of α-TTF-DPNI and TTN-DPNI. Both α-TTF-DPNI and TTN-DPNI could be prepared mechanochemically and in high phase-purity by grinding powders of the donor (TTF or TTN, respectively) with an equimolar amount of DPNI. This suggests a facile synthetic route to achieving large scale preparation of these CT complexes required for bulk characterisation. The process was easily monitored by eye due to the vivid colour change to bright green or black for α-TTF-DPNI and TTN-DPNI, respectively (note: the colours of the precursors TTF, TTN and DPNI are orange, tan and beige, respectively). The PXRD patterns of the mechanochemically-prepared bulk powders were highly crystalline and corresponded well with their simulated PXRD patterns calculated from their respective crystal structures (Figure S4 for α-TTF-DPNI, Figure S5 for TTN-DPNI, ESI).

Electronic properties of D and A components. The HOMO and LUMO energies of the D and A components, respectively, were probed using cyclic voltammetry (Figure S6, ESI). The DPNI acceptor moiety exhibited two reversible reduction processes, corresponding to the generation of radical anion state ($E_{1/2} = -0.98$ *vs.* Fc/Fc$^+$) and dianion states (-1.47 V *vs.* Fc/Fc$^+$) of NDI. TTF exhibits two highly reversible oxidation processes at mild potentials of $E_{1/2} = -0.02$ and $+0.22$ V *vs.* Fc/Fc$^+$, characteristic of the TTF/TTF$^{·+}$ and TTF$^{·+}$/TTF^{2+} redox couples, respectively. The related compound TTN, known to be a weaker electron donor than TTF, exhibited a *quasi*-reversible oxidation wave at $E_{pc} = +0.50$ V *vs.* Fc/Fc$^+$ attributed to the

oxidation of TTN to its radical cation state, followed by a reversible process at $E_{1/2}$ = +0.77 V *vs.* Fc/Fc^+ characteristic of the subsequent oxidation to its dication state.

The ionisation potentials (IPs) of the donors (TTF and TTN) and the electron affinities (EAs) of the acceptor (DPNI) were determined using the M06-2X functional combined with the 6-311+G(3df,2p) basis set to further support the relative redox potentials of the framework components as determined by CV (Table 1). The trend observed with the electron donors was clearly demonstrated, whereby TTF, the better electron donor, has a lower IP than TTN. In comparison, the IPs of the donor molecules are significantly higher than the EAs of the pillaring ligands which, consequently, results in non-optimal redox matching between D and A units. This poor overlap in the D and A frontier energy levels is consistent with the structural characteristics of the TTF and TTN in these CT complexes, which suggest that these donor moieties are in their neutral states.

Table 1. Electrochemical data for TTF, TTN and DPNI determined by CV (electrolyte: [(n-C_4H_9)$_4$N]PF$_6$ (0.1 M) in DMF)) as well as DFT calculated IPs and EAs of donors and acceptors, respectively.

Component	Redox process 1 (V *vs.* Fc/Fc^+)	Redox process 2 (V *vs.* Fc/Fc^+)	IP (eV)	EA (eV)
TTF	−0.02	+0.22	5.30	-
TTN	+0.50	+0.77	5.53	-
DPNI	−0.98	−1.47	-	3.87

Optical properties *via* a combined experimental and computational approach. The optical properties of α-TTF-DPNI and β-TTF-DPNI were characterised by solid state diffuse reflectance UV–Vis–NIR spectroscopy and compared to the spectra of its precursors (Figure 3a). The spectra of the two CT complexes have a distinct band at 11500 cm^{-1}, which does not correspond to features of TTF or DPNI alone and is assigned to CT between TTF and DPNI units. The diffuse reflectance spectrum of TTN-DPNI was compared to the spectra of discrete TTN and DPNI. Two broad bands at 11700 and 18500 cm^{-1}, which are absent in the spectra of its donor and acceptor precursors (Figure 3b), were ascribed to CT between TTN and DPNI.
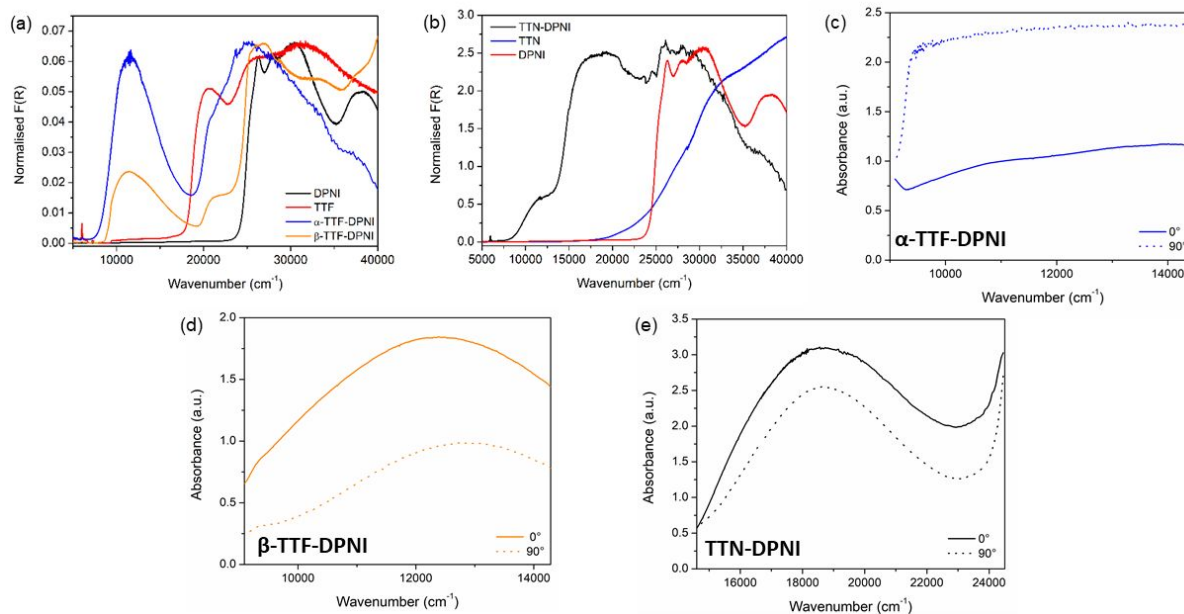
Figure 3. Solid state diffuse reflectance UV–Vis–NIR of (a) α-TTF-DPNI, β-TTF-DPNI and its components TTF and DPNI, and (b) TTN-DPNI and its precursors TTN and DPNI. Single-crystal spectra of (c) α-TTF-DPNI in the NIR region (d) β-TTF-DPNI in the NIR region and (e) TTN-DPNI in the visible region.

The dichroic behaviour of these CT complexes led to the analysis of the optical spectra of the single crystals as a function of polarisation. There are similarities in the NIR regions of the spectra for both α-TTF-DPNI and β-TTF-DPNI. Upon polarisation, α-TTF-DPNI exhibits an increase in the broad CT band at 11500 cm^{-1} upon polarisation (Figure 3c), while β-TTF-DPNI shows a more modest decrease in its broad CT band (Figure 3d). The variation in band intensity suggests that both complexes exhibit dichroism, but only that of α-TTF-DPNI can be observed by eye. Dichroism is also noticeable in the visible spectra of α-TTF-DPNI *vs.* β-TTF-DPNI (Figure S7, ESI); specifically, a shoulder band at 21000 cm^{-1} is lost in the spectrum of α-TTF-DPNI upon polarisation and does not appear in the corresponding β-TTF-DPNI complex. The TTN-DPNI CT complex exhibits greater resolution of the bands in the visible region of its spectrum (Figure 3e). Upon rotation of the TTN-DPNI CT crystal, changes in the CT band at 18500 cm^{-1} (Figure 3e) suggest dichromic behaviour. Negligible changes are observed in the NIR spectral regions of TTN-DPNI (Figure S8, ESI).

UV–Vis–NIR absorption behaviours were computationally examined using TTF-DPNI and TTN-DPNI dimer models, with geometries extracted selectively from the crystal structures (Figure 4). In this case, low-energy absorptions were found in the dimeric structures which are

absent in the spectra of the individual components. The occurrence of these bands depends not only on the proximity between the donor and acceptor species but also on the relative orientations between them.
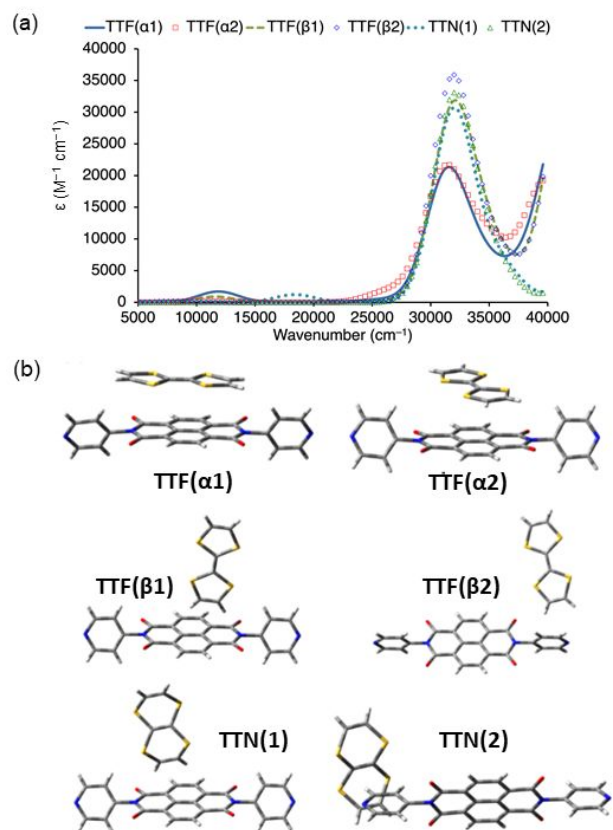

Figure 4. (a) Calculated UV–Vis–NIR spectra of dimeric models for α-TTF-DPNI, β-TTF-DPNI and TTN-DPNI, and the (b) corresponding dimeric models used for each spectrum.

Inspection of the orbitals involved in the low-energy transitions in the dimers show that they correspond to charge transfer from the TTF or TTN donors to the NDI core of the DPNI acceptor. This is consistent with the occurrences of these CT bands only when the TTF or TTN donors are close to the core of the acceptor (TTF(α1), TTF(β1) and TTN(1) in Figure 4b) rather than towards the pyridine moiety (TTF(β2) and TTN(2)). The reason as to why CT occurs in the TTF(α1) orientation but not in the TTF(α2) orientation is less clear. For those orientations not observing CT interactions (TTF(α2), TTF(β2) and TTN(2)), the relative energies are qualitatively consistent with the calculated IPs of TTF and TTN (Table 1), such that α- and β-TTF-DPNI have similar peak positions, but the major TTN-DPNI CT peak occurs at a higher-energy position. The relatively low intensities of the calculated CT bands can be rationalised

by the large gaps between the donor IPs and the acceptor EA. The comparatively more intense low-energy absorption observed experimentally thus suggests that the *extended* crystalline packing and sheet-like structure of TTF or TTN and DPNI moieties significantly enhances CT in these complexes.

Vibrational spectroscopy for CT determination. Solid state Raman spectroscopy is a powerful technique for probing the redox states of electroactive species and has been widely employed in the characterisation of ρ in CT complexes.[55-59] For example, work by Matsuzaki and colleagues reported on the Raman frequencies of TTF in its neutral and radical cation states, as well as in CT complexes such as TTF-TCNQ and the TTF-halide series of materials where TTF is partially charged.[55] A clear dependence of the Raman frequencies of TTF as a function of its charge was elucidated.

In this present work, the vibrational modes of TTF, TTN and DPNI were studied to gain insight into the redox states present inside these CT complexes. Raman spectra were collected for all three CT complexes. Raman spectra of α- and β-TTF-DPNI showed small differences between the two phases, whereby the bands observed in the β-phase are higher in energy by up to 15 cm^{-1} (Figure 5a). Comparatively, there is an absence of Raman characterisation of the TTN moiety and its CT complexes. Unlike the TTF CT complexes, where the Raman spectra exhibit strong vibrations from both moieties, the Raman spectrum of TTN-DPNI is largely dominated by the Raman features due to DPNI (Figure 5b).
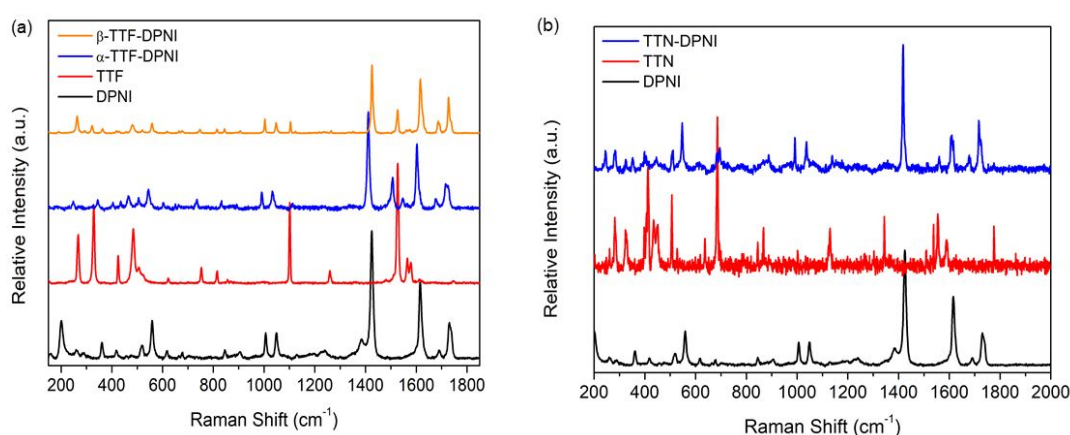
Figure 5. Confocal Raman spectra of (a) α-TTF-DPNI, β-TTF-DPNI, TTF and DPNI, and (b) TTN-DPNI, TTN, and DPNI under 785 nm laser excitation. Background subtraction was performed on these spectra to remove fluorescence contributions.

All spectroscopic assignments for the three CT complexes were supported by DFT calculations. This is particularly important for TTN and TTN-DPNI, where there is a significant gap in the literature on the shift in Raman frequencies of TTN as a function of its redox state. The bands assigned to TTF largely correlated with the spectrum of neutral TTF (Table 2), suggesting that the degree of charge transfer in these materials is essentially zero. This is consistent with structural data and DFT calculations for the TTF-DPNI and TTN-DPNI dimers, which show minimal CT in the range of 0.007-0.036 electrons. While the spectra for α- and β-TTF-DPNI differ only slightly, a notable and clear distinction is in the intensity of the peak at approximately 1100 cm^{-1}. DFT calculations reveal that this corresponds to a bending mode of the terminal C-H bonds for the TTF molecule (Figure S9, ESI). In β-TTF-DPNI, the TTF molecules are arranged in a parallel fashion, and thus the shape-changes of these ellipsoids add to one another, leading to a Raman active absorption. In comparison, in α-TTF-DPNI, there are two sets of TTF molecules that run more-or-less perpendicular to one another. This leads to cancellation of the ellipsoid shape-change in an overall manner for this C-H bending mode, and as a result, it becomes less active in the Raman spectrum.

Table 2. Raman frequencies of TTF, α-TTF-DPNI, β-TTF-DPNI and TTN-DPNI obtained under 785 nm laser excitation. Values for TTF^0 and TTF$^{•+}$ (*) were reported by Matsuzaki and co-workers,[55] while DFT for TTN and the TTN radical cation were calculated for the first time.

Band	Raman Shifts (cm^{-1})				
	TTF*	**TTF$^{•+}$***	**TTF**	**α-TTF-DPNI**	**β-TTF-DPNI**
υ_2	1553	1508	1564	1547	1561
υ_3	1516	1420	1527	1507	1527
υ_4	1089	-	1101	-	1105
υ_5	741	761	753	736	748
υ_6	472	509	484	468	480
υ_7	253	268	267	248	263
	TTN^0	**TTN$^{•+}$**	**TTN**	**TTN-DPNI**	

ν_2	270	290	282	283	-
ν_3	313	-	324	324	-
ν_4	422	433	412, 435, 450	398, 405, 445	-
ν_5	492	499	506	-	-
ν_6	657	656, 684	686	684, 695	-
ν_7	767	781	845,868	-	-
ν_8	1127	-	1130	1138	-
ν_9	1257	-	1344	-	-
ν_{10}	1517, 1577	1387	1538, 1555, 1589	1514, 1561	-
ν_{11}	-	1568	1776	-	-

Vibrational energies of TTN^0 and $TTN^{\bullet+}$ were calculated for the first time. The calculated Raman frequencies of neutral TTN were in good agreement with the experimental spectrum obtained under 785 nm laser excitation (Table 2). The calculated spectrum for $TTN^{\bullet+}$ is strikingly different from its neutral counterpart in the fewer number of peaks; this may be a result of increased planarity and therefore symmetry of the molecule upon oxidation which would result in a change from C_{2h} (chair) to D_{2h} symmetry (planar).[54] A comparison of the vibrational shifts of TTN-DPNI with the calculated and experimental shifts of TTN^0 shows a good correlation between the energies of their vibrational modes. The most prominent signature in the calculated spectrum of $TTN^{\bullet+}$ that discriminates it against neutral TTN is a strong peak at 1387 cm^{-1}. The absence of this peak in the spectrum of TTN-DPNI further suggests that TTN is in its neutral state.

Radical characteristics determined by EPR. Room temperature X-band EPR measurements performed on mechanochemically synthesised, polycrystalline samples of α-TTF-DPNI, β-TTF-DPNI and TTN-DPNI detected organic radicals (Figure 6). The very low intensity associated with each EPR signal is consistent with the low degree of partial charge transfer in these CT complexes as determined by structural analysis, Raman spectroscopy and DFT

studies. Simulations of the EPR profiles of α-TTF-DPNI and β-TTF-DPNI, which are almost identical, can be fitted to two $S = \frac{1}{2}$ spins, one with rhombic anisotropy ($g_x = 2.0120$, $g_y = 2.0081$, $g_y = 2.0045$), interacting with two proton nuclei attributed to the TTF radical cation, and an anisotropic signal at $g_{iso} = 2.0010$ assigned to the DPNI radical anion (Figure S10, ESI). The spectrum of TTN-DPNI can also be modelled as two $S = \frac{1}{2}$ spins at $g_{iso} = 2.0047$ and 2.0015 (Figure S11, ESI), the former which weakly interacts with a proton nucleus and may be assigned to the TTN radical cation, whilst the latter is due to the DPNI radical anion. The weak interaction of the TTN radical cation with only one proton nucleus is consistent with its chair configuration, suggesting low electron delocalisation across the donor core. The two radical species found in each CT complex further lend support to the presence of partial charge transfer in these systems.
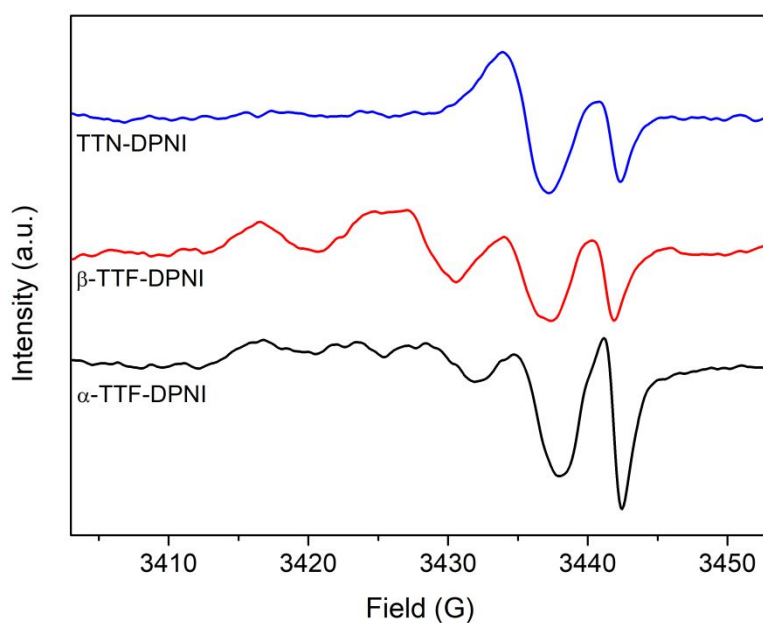
Figure 6. Room temperature X-band EPR of α-TTF-DPNI, β-TTF-DPNI and TTN-DPNI.

Bulk conductivity. The bulk conductivities of α-TTF-DPNI and TTN-DPNI were measured *via* the two-probe method on pressed pellets of the mechanochemically synthesised powders. TTN-DPNI exhibited three orders of magnitude greater conductivity than α-TTF-DPNI (5×10^{-11} and 2×10^{-8} S cm^{-1}, respectively) despite the poorer redox match between TTN and DPNI (Figure S12, ESI). This suggests that the segregated stacking arrangement outweighs the slightly poorer redox match in D and A in facilitating conductivity. Along this vein, the

isostructure β-TTF-DPNI is expected to exhibit the highest conductivity amongst these three materials; however, the lack of a facile synthesis of this compound prohibited its measurement. Overall, these values were in the range for insulating materials; this was expected owing to the low ρ in these systems and thus, the limited charge carriers which would promote conductivity. Furthermore, the *quasi*-1D nature of the D–A stacks responsible for the crystal's dichroism, is indicative of the anisotropy of the CT behaviour in α-TTF-DPNI, which is expected to be reflected in its conductivity. Efforts to obtain single crystal conductivity parallel and perpendicular to the direction of the D–A stacks were unsuccessful due high resistance (likely accentuated from internal cracking of the crystal).

CONCLUSIONS

A series of three CT complexes, α-TTF-DPNI, β-TTF-DPNI and TTN-DPNI, were synthesised by solution and mechanochemical methods, then characterised by a combined experimental and theoretical approach to elucidate the charge transfer character in these closely related materials. The degree of CT in these systems is close to zero (0.007-0.036 electrons as calculated by DFT); however, their optical spectra show new low energy transitions attributable to partial charge transfer from the TTF and TTN donors to the DPNI acceptor. α-TTF-DPNI and β-TTF-DPNI, which have the same chemical composition but differ in donor/acceptor organisation i.e., mixed *vs.* segregated stack, respectively, share a CT band at 11500 cm^{-1} due to the IP and EA of their constituents. TTN-DPNI, which is isomorphic to β-TTF-DPNI, has two CT bands at higher energies as a result of the higher IP of TTN compared to TTF. Consideration of the TTF bond lengths *via* SCXRD, Raman spectroscopy and DFT calculations suggested charge neutrality in the donor molecule; however the high sensitivity of EPR could detect low concentrations of two radical species in each CT complex, likely resulting from the CT phenomenon. This combined approach highlights the utility of a range of spectroscopies to understand the nature of charge transfer interactions in the solid state.

ACKNOWLEDGEMENTS

1
2
3
4
5
6
7
8
9
10
11
12
13
14
15
16
17
18
19
20
21
22
23
24
25
26
27
28
29
30
31
32
33
34
35
36
37
38
39
40
41
42
43
44
45
46
47
48
49
50
51
52
53
54
55
56
57
58
59
60

REFERENCES

1.   U. M. Rabie, *Journal of Molecular Structure*, 2013, **1034**, 393-403.
2.   M. Mohammadtaheri, R. Ramanathan and V. Bansal, *Catalysis Today*, 2016, **278**, 319-329.
3.   G. E. M. Crisenza, D. Mazzarella and P. Melchiorre, *Journal of the American Chemical Society*, 2020, **142**, 5461-5476.
4.   K. Medjanik, H.-J. Elmers, G. Schönhense, J.-P. Pouget, R. Valenti and M. Lang, 2019, **256**, 1800745.
5.   J. Ferraris, D. O. Cowan, V. Walatka and J. H. Perlstein, *Journal of the American Chemical Society*, 1973, **95**, 948-949.
6.   S. E. Brown, *Physica C: Superconductivity and its Applications*, 2015, **514**, 279-289.
7.   S. Hünig and P. Erk, 1991, **3**, 225-236.
8.   J. L. Segura and N. Martín, 2001, **40**, 1372-1409.
9.   D. Canevet, M. Sallé, G. Zhang, D. Zhang and D. Zhu, *Chemical Communications*, 2009, DOI: 10.1039/B818607N, 2245-2269.
10.   J. B. Torrance, J. E. Vazquez, J. J. Mayerle and V. Y. Lee, *Physical Review Letters*, 1981, **46**, 253-257.
11.   R. Chen, M. K. Gokus and S. Pagola, 2020, **10**, 482.
12.   S. H. Lapidus, A. Naik, A. Wixtrom, N. E. Massa, V. Ta Phuoc, L. del Campo, S. Lebègue, J. G. Ángyán, T. Abdel-Fattah and S. Pagola, *Crystal Growth & Design*, 2014, **14**, 91-100.
13.   A. Wixtrom, J. Buhler and T. Abdel-Fattah, *Journal of Chemical Education*, 2014, **91**, 1232-1235.
14.   S. Benjamin, S. Pagola, Z. Huba, E. Carpenter and T. Abdel-Fattah, *Synthetic Metals*, 2011, **161**, 996-1000.
15.   A. Graja, A. Brau, J. P. Farges, M. Golub, A. Tracz and J. K. Jeszka, *Synthetic Metals*, 2001, **120**, 753-754.
16.   I. Smirani, R. Lipiec, A. Brau, J. P. Farges and A. Graja, *Journal of Materials Science*, 2001, **36**, 1227-1230.
17.   E. Krausz, *Aust. J. Chem.*, 1993, **46**, 1041-1054.
18.   E. Krausz, *AOS News*, 1998, **12**, 21-24.
19.   P. W. Doheny, J. K. Clegg, F. Tuna, D. Collison, C. J. Kepert and D. M. D'Alessandro, *Chemical Science*, 2020, **11**, 5213-5220.
20.   J. Riga, J. J. Verbist, F. Wudl and A. Kruger, 1978, **69**, 3221-3231.
21.   S. I. Nakatsuji, Y. Amano, H. Kawamura and H. Anzai, *Liebigs Annalen*, 1997, **1997**, 729-732.
22.   Y. Sun, Z. Cui, L. Chen, X. Lu, Y. Wu, H.-L. Zhang and X. Shao, *RSC Advances*, 2016, **6**, 79978-79986.

23.   M. A. Kobaisi, R. S. Bhosale, M. E. El-Khouly, D. D. La, S. D. Padghan, S. V. Bhosale, L. A. Jones, F. Antolasic, S. Fukuzumi and S. V. Bhosale, *Scientific Reports*, 2017, **7**, 16501.

24.   T. Ono, Y. Tsukiyama, A. Taema and Y. Hisaeda, *Chemistry Letters*, 2017, **46**, 801-804.

25.   M. Pan, X.-M. Lin, G.-B. Li and C.-Y. Su, *Coordination Chemistry Reviews*, 2011, **255**, 1921-1936.

26.   A. Das and S. Ghosh, *Angewandte Chemie International Edition*, 2014, **53**, 2038-2054.

27.   S. Saha, *Accounts of Chemical Research*, 2018, **51**, 2225-2236.

28.   Y. Zhou and L. Han, *Coordination Chemistry Reviews*, 2021, **430**, 213665.

29.   C. Kulkarni, G. Periyasamy, S. Balasubramanian and S. J. George, *Physical Chemistry Chemical Physics*, 2014, **16**, 14661-14664.

30.   J.-J. Liu, T. Liu, S.-B. Xia, C.-X. He, F.-X. Cheng, M.-J. Lin and C.-C. Huang, *Dyes and Pigments*, 2018, **149**, 59-64.

31.   P. Lasitha, *Photochemical & Photobiological Sciences*, 2020, **19**, 1603-1612.

32.   S. Guha and S. Saha, *Journal of the American Chemical Society*, 2010, **132**, 17674-17677.

33.   K. S. Varma, N. Sasaki, R. A. Clark, A. E. Underhill, O. Simonsen, J. Becher and S. Bøwadt, *Journal of Heterocyclic Chemistry*, 1988, **25**, 783-787.

34.   Bruker, *SAINT*, Bruker AXS Inc., Madison, Wisconsin, USA, 2012.

35.   G. M. Sheldrick, *Program for Crystal Structure solution*, Institüt für Anorganische Chemie der Universität, Tammanstrasse 4, D-3400 Göttingen, Germany, 1986.

36.   G. Sheldrick, *Acta Crystallographica Section C*, 2015, **71**, 3-8.

37.   O. V. Dolomanov, L. J. Bourhis, R. J. Gildea, J. A. K. Howard and H. Puschmann, *Journal of Applied Crystallography*, 2009, **42**, 339-341.

38.   Agilent, *CrysAlis PRO*, Agilent Technologies Ltd, Yarnton, Oxfordshire, England, 2014.

39.   L. Farrugia, *Journal of Applied Crystallography*, 2012, **45**, 849-854.

40.   A. Technologies, *SCALE3 ABSPACK CrysAlisPro*, Agilent Technologies UK Ltd., Oxford, England, 2011-2013.

41.   W. Koch and M. C. Holthausen, in *A Chemist's Guide to Density Functional Theory*, Wiley New York, 2nd edn., 2001, DOI: https://doi.org/10.1002/3527600043.fmatter_indsub.

42.   M. J. Frisch, G. W. Trucks, H. B. Schlegel, G. E. Scuseria, M. A. Robb, J. R. Cheeseman, G. Scalmani, V. Barone, G. A. Petersson, H. Nakatsuji, X. Li, M. Caricato, A. V. Marenich, J. Bloino, B. G. Janesko, R. Gomperts, B. Mennucci, H. P. Hratchian, J. V. Ortiz, A. F. Izmaylov, J. L. Sonnenberg, Williams, F. Ding, F. Lipparini, F. Egidi, J. Goings, B. Peng, A. Petrone, T. Henderson, D. Ranasinghe, V. G. Zakrzewski, J. Gao, N. Rega, G. Zheng, W. Liang, M. Hada, M. Ehara, K. Toyota, R. Fukuda, J. Hasegawa, M. Ishida, T. Nakajima, Y. Honda, O. Kitao, H. Nakai, T. Vreven, K. Throssell, J. A. Montgomery Jr., J. E. Peralta, F. Ogliaro, M. J. Bearpark, J. J. Heyd, E. N. Brothers, K. N. Kudin, V. N. Staroverov, T. A. Keith, R. Kobayashi, J. Normand, K. Raghavachari, A. P. Rendell, J. C. Burant, S. S. Iyengar, J. Tomasi, M. Cossi, J. M. Millam, M. Klene, C. Adamo, R. Cammi, J. W. Ochterski, R. L. Martin, K. Morokuma, O. Farkas, J. B. Foresman and D. J. Fox, *Gaussian 16 Rev C.01*, 2016.

43.   P. J. Stephens, F. J. Devlin, C. F. Chabalowski and M. J. Frisch, *The Journal of Physical Chemistry*, 1994, **98**, 11623-11627.

44.   B. Chan, 2017, **89**, 699-713.

45.　B. Chan, A. Karton and K. Raghavachari, *Journal of Chemical Theory and Computation*, 2019, **15**, 4478-4484.

46.　Y. Zhao and D. G. Truhlar, *Theoretical Chemistry Accounts*, 2008, **120**, 215-241.

47.　N. Mardirossian and M. Head-Gordon, *Molecular Physics*, 2017, **115**, 2315-2372.

48.　A. D. Boese and J. M. Martin, *J Chem Phys*, 2004, **121**, 3405-3416.

49.　F. Trani, G. Scalmani, G. Zheng, I. Carnimeo, M. J. Frisch and V. Barone, *Journal of Chemical Theory and Computation*, 2011, **7**, 3304-3313.

50.　C. F. Leong, B. Chan, T. B. Faust, P. Turner and D. M. D'Alessandro, *Inorganic Chemistry*, 2013, **52**, 14246-14252.

51.　F. J. Rizzuto, T. B. Faust, B. Chan, C. Hua, D. M. D'Alessandro and C. J. Kepert, 2014, **20**, 17597-17605.

52.　T. J. Kistenmacher, M. Rossi, C. C. Chiang, R. P. Van Duyne and A. R. Siedle, *Inorganic Chemistry*, 1980, **19**, 3604-3608.

53.　M. Bousseau, L. Valade, J. P. Legros, P. Cassoux, M. Garbauskas and L. V. Interrante, *Journal of the American Chemical Society*, 1986, **108**, 1908-1916.

54.　H. Bock, B. Roth, M. V. Lakshmikantham and M. P. Cava, *Phosphorus and Sulfur and the Related Elements*, 1984, **21**, 67-77.

55.　S. Matsuzaki, T. Moriyama and K. Toyoda, *Solid State Communications*, 1980, **34**, 857-859.

56.　R. P. Van Duyne, T. W. Cape, M. R. Suchanski and A. R. Siedle, *The Journal of Physical Chemistry*, 1986, **90**, 739-743.

57.　S. Sweetnam, K. Vandewal, E. Cho, C. Risko, V. Coropceanu, A. Salleo, J.-L. Brédas and M. D. McGehee, *Chemistry of Materials*, 2016, **28**, 1446-1452.

58.　A. Salmerón-Valverde and S. Bernès, *CrystEngComm*, 2015, **17**, 6227-6235.

59.　H.-D. Wu, F.-X. Wang, M. Zhang and G.-B. Pan, *Nanoscale*, 2015, **7**, 12839-12842.